Vdovin G. K., Rudenko A. O., Antonov B. D.,
Malkov V. B., Demin A. K., Medvedev D. A.
Chimica Techno Acta. 2019. Vol. 6, No. 2. P. 38–45.
ISSN 2409–5613

DOI: 10.15826/chimtech.2019.6.2.01

G. K. Vdovin[a], A. O. Rudenko[a], B. D. Antonov[a], V. B. Malkov[a], A. K. Demin[ab], D. A. Medvedev[ab]

[a] *Institute of High Temperature Electrochemistry, Yekaterinburg 620990, Russia*
[b] *Graduate School of Economics and Management, Ural Federal University, Yekaterinburg 620002, Russia*
e-mail: dmitrymedv@mail.ru

Manipulating the grain boundary properties of $BaCeO_3$-based ceramic materials through sintering additives introduction

$BaCeO_3$-based materials represent a well-known family of proton-conducting electrolytes, which can be used in different solid oxide electrochemical devices. An effective operation of the latter across an intermediate-temperature range requires improved transport of PCEs, including their grain (G) and grain boundary (GB) components. In the present work, some 3d-elements in a small amount were used as sintering additives to verify the possibility of improving the GB conductivity of $BaCe_{0.9}Gd_{0.1}O_{3-\delta}$. It is shown that copper oxide (CuO) can be considered as one of the most effective sintering agents, since its use enables decreasing the GB density of the BCG ceramic material at the reduced sintering temperatures. The obtained results form a new tactic for designing new protonic electrolytes, whose conductivity might be prevail over ones containing Ni-based modifiers.

Keywords: $BaCeO_3$; SOFCs; SOECs; sintering additives; impedance spectroscopy; proton-conducting electrolytes.

Received: 11.06.2019. Accepted: 28.06.2019. Published: 05.08.2019.

Introduction

Proton-conducting oxide (PCO) materials occupy a special place in the high-temperature electrochemistry due to its unique features consisting in proton transportation in an oxide matrix [1–5]. These features allows PCOs to be utilized as electrolytes for various types of electrochemical devices (EDs) such as solid oxide fuel cells (SOFCs), solid oxide electrolysis cells (SOECs), pumps and sensors [6–9]. As a result of high realizable conductivity levels of PCOs, the mentioned devices can operate at reduced temperatures (below 600 °C) compared with the conventional systems based on oxygen-ionic electrolytes [10, 11].

In order to further improve the EDs' performance and efficiency, different strategies aimed at the electrolyte modifications can be exploited [1–3, 12–14]: the decrease of their thickness, designing the structures with a higher ionic mobility, purposeful modification of ceramics morphology. The latter is a highly promising strategy, since the overall conductivity of polycrystalline PCOs is known to be determined by a high resistance of grain boundaries [14]. One of the most obvious

ways to modify the grain boundaries rests on adding the low-melting phases [15], which intensify mass transport and promotes grain growth. Nickel oxide (NiO) is often used as such an additive. However, no improvement (or even deterioration) of grain boundary transport is observed [16–20]; this is due to two undesirable effects: very low solubility of Ni^{2+}-ions in a Ce-sublattice of $BaCeO_3$-based materials and, consequently, the sedimentation of proton-blocking Ni-containing phases (NiO, BaY_2NiO_5) along the grain boundaries. Therefore, a rational search of possible alternative to NiO is a matter of fundamental and applied interests associated, respectively, with design of PCOs with optimized properties and their successful application in EDs.

In the present work, on a well-known example of PCOs, $BaCe_{0.9}Gd_{0.1}O_{3-\delta}$, possibility of improving its grain boundary transport was checked via an addition of CuO, Co_3O_4 and NiO as second dopants. To launch bridges between structural, microstructural and transport properties of the materials obtained, the X-ray diffraction (XRD), scanning electron microscopy (SEM) and electrochemical impedance spectroscopy (EIS) analyses were used.

Experimental

$BaCe_{0.9}Gd_{0.1}O_{3-\delta}$ (BCG) material and its doping derivatives ($BaCe_{0.89}Gd_{0.1}M_{0.01}O_{3-\delta}$, BCGM, where M = Cu, Co and Ni) were prepared using traditional solid state synthesis method. $BaCO_3$, CeO_2, Gd_2O_3, CuO, Co_3O_4 and NiO powders (with purity not less than 99.5%) were taken in stoichiometric amounts and thoroughly mixed via a mortar and pestle. The obtained mixtures were first pre-synthesized at 1100 °C for 5 h. The resulting powders were again mechanically activated, uniaxally pressed into discs and then sintered at 1450 °C for 3 h.

One part of the obtained ceramic samples was crushed and characterized by XRD (diffractometer Rigaku D/MAX-2200VL/PC, Japan), while another part was studied by SEM (JEOL JSM-5900 LV, Japan).

Electrochemical characterization was performed for the Ag|BCG|Ag or Ag|BCGM|Ag symmetrical cells by utilizing an Amel 2550 potentiostat/galvanostat (Italy) and a MaterialsM 520 frequency response analyser (Italy). These cells were fabricated in the following sequence: polishing the discs, an Ag paste painting and its sintering at 800 °C for 1 h. The impedance spectra were obtained for wet (pH_2O = 0.03 atm) air atmosphere in a frequency range of 10^{-2}–10^6 Hz with an amplitude of 30 mV. The spectra were analysed by an equivalent circuit method, using a ZView software for model processing.

Results and discussion

The XRD pattern of the sintered BCG material (Fig. 1) shows the formation of a single-phase product, the crystal structure of which can be indexed as an orthorhombically-distorted perovskite with lattice parameters of a = 6.221 Å, b = 8.770 Å, c = 6.244 Å and space group of *Pmcn*. The doping with 3d-elements does not change symmetry of the perovskite structure, while the lattice parameters of BCGM are virtually constant (a = 6.220 ± 0.003 Å, b = 8.766 ± 0.005 Å, c = 6.237 ± 0.007 Å). These results can be explained by the extremely small amount of sintering additives introduced into the $BaCeO_3$ structure, 0.005 mol.%.

Despite of small concentrations used, the M-doping affects considerably the microstructural parameters of the sintered materials that can be seen from qualitative (Fig. 2) and quantitative (Table 1) analyses. In detail, the processes associated with grains growth, their close package, pores disappearance and densification occur in all the cases. Nevertheless, a degree of these processes is different and increases in the sequence of BCGCo–BCGCu–BCGNi, indicating dissimilar nature of the sintering additives.

To reveal grain ($\sigma_{g.}$) and grain boundary ($\sigma_{g.b.}$) contributions of the total conductivity (σ_{total}), the EIS analysis was successfully performed. The electrochemical characterization was carried out in different tem-

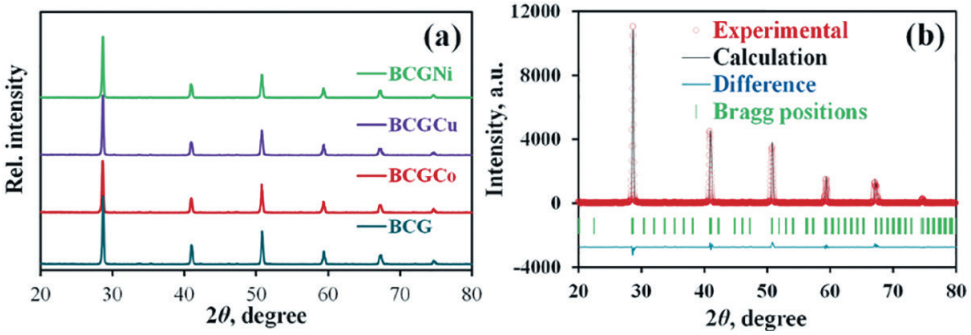

Fig. 1. XRD patterns of the sintered BCG and BCGM materials (a) and example of refinement for BCG (b)

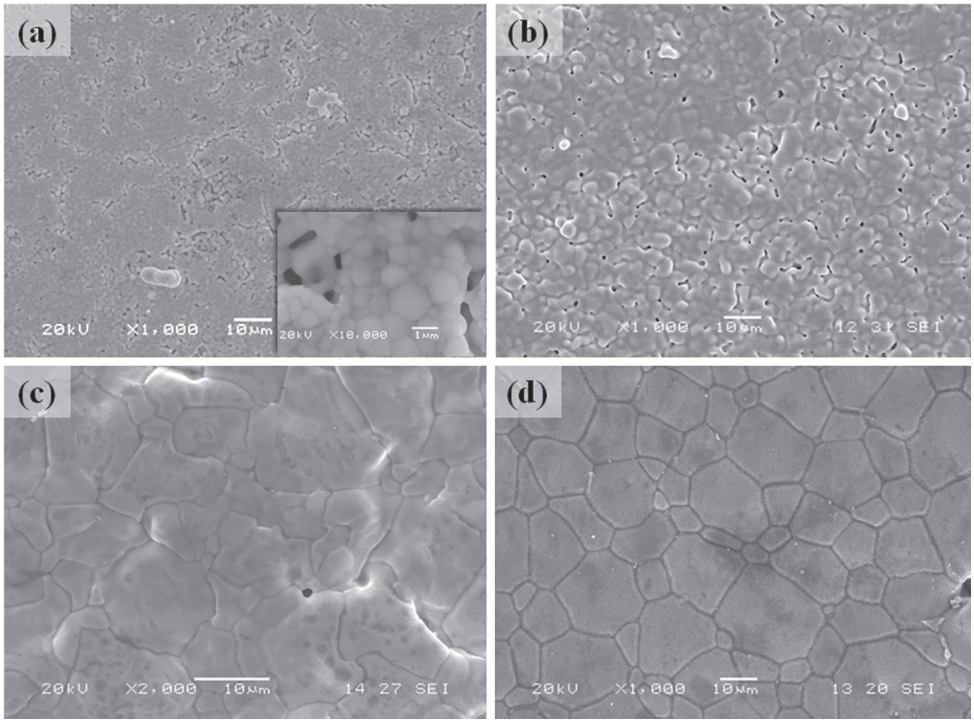

Fig. 2. Surface morphology of the sintered ceramic materials: BCG (a), BCGCo (b), BCGCu (c) and BCGNi (d)

Table 1

Microstructural parameters of the BCG and BCGM materials sintered at 1450 °C for 3 h: ρ is the relative density, *L* is the total shrinkage, *D* is the average grain size, γ is the grain boundary density [a]

Composition	ρ, %	*L*, %	*D* ± 5%, μm	γ ± 5%, μm^{-1}
BCG	86	8.2	0.8	4.66
BCGCo	91	12.3	3.4	1.10
BCGCu	94	17.5	6.9	0.54
BCGNi	97	22.3	9.6	0.39

[a] estimated on the base of the following equation: $\gamma = 3.722 \cdot D^{-1}$, see ref. [21].

perature ranges, boundaries of which were determined by accuracy of the analysis. The obtained spectra (Fig. 3) were analyzed using an equivalent circuit scheme of R_o–(R_1Q_1)–(R_2Q_2)–(R_3Q_3), where *R* is the resistance, *Q* is the constant phase element, indexes of 1, 2, 3 correspond to grain, grain boundary and electrode processes, respectively. Correlation of hodographs' elements with these processes is performed analyzing the characteristic capacitance (*C*) and frequency (*f*) values calculated as follows:

$$C = (R \cdot Q)^{1/n} \cdot R^{-1} \quad (1)$$

$$f = (R \cdot Q)^{-1/n} \cdot (2\pi)^{-1} \quad (2)$$

Here, *n* is the power index in a frequency dependence part of the constant phase element. Depending on the temperature, the *C* value varies between 20 and 80 pF for the first arc and between 3 and 8 nF for the second one, while the *f* values amount hundreds kHz and hundreds Hz, respectively. Both levels of these parameters relate with grain and grain boundary properties.

It should be noted that R_o = 0.001 Ω was purposefully introduced in the equivalent circuit scheme; it imitates the origin of the coordinates, providing a correct fitting.

As can be seen from Fig. 4a, Cu- and Ni-doping of BCG results in an increase of $\sigma_{g.}$, while Co-doping has an opposite (but minor) effect. For example, the $\sigma_{g.}$ value at 200 °C reaches $5.01 \cdot 10^{-5}$, $3.27 \cdot 10^{-5}$ and $2.61 \cdot 10^{-4}$ S cm^{-1} for BCG, BCGCo and BCGCu, respectively. This parameter cannot be precisely determined for the BCGNi material at 200 °C, but its $\sigma_{g.}$ level is by ~2 times lower than that of BCGCu at the lower temperatures (100–150 °C).

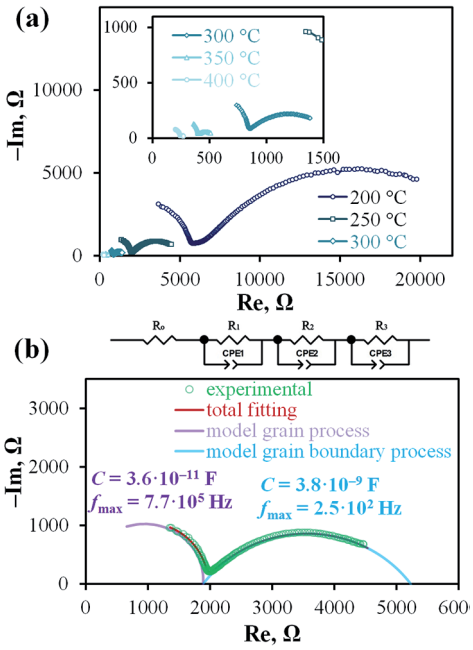

Fig. 3. Impedance spectra obtained for the Ag|BCG|Ag symmetrical cell at different temperatures in wet air atmosphere (a) and example of the fitting procedure for the spectra obtained at 250 °C (b)

Discussing the grain boundary transport (Fig. 4*b*), the $\sigma_{g.b.}$ improvement is observed for all the BCG-modified materials and can be related with decreasing the grain boundary density (Table 1). Comparison of the BCGCu and BCGNi samples allows formulation of the assumption that nickel is only partially dissolved in the Ce-sublattice of BCG, while another part localizes onto grain boundaries. This proposal is based on the fact that BCGNi exhibits the lowest grain boundary density, which should provide the highest $\sigma_{g.b.}$; however, this is not confirmed experimentally.

The resulting conductivity (σ_{total}, Fig. 4*c*) of the BCGM samples is higher than that of BCG, showing that the grain boundary transport determines the overall properties even for BCGCo (at least in the entire studied temperature range). The BCGCu material exhibits the maximal achievable σ_{total} values, ranging from $6.33 \cdot 10^{-6}$ S cm^{-1} at 100 °C to $1.86 \cdot 10^{-4}$ S cm^{-1} at 200 °C.

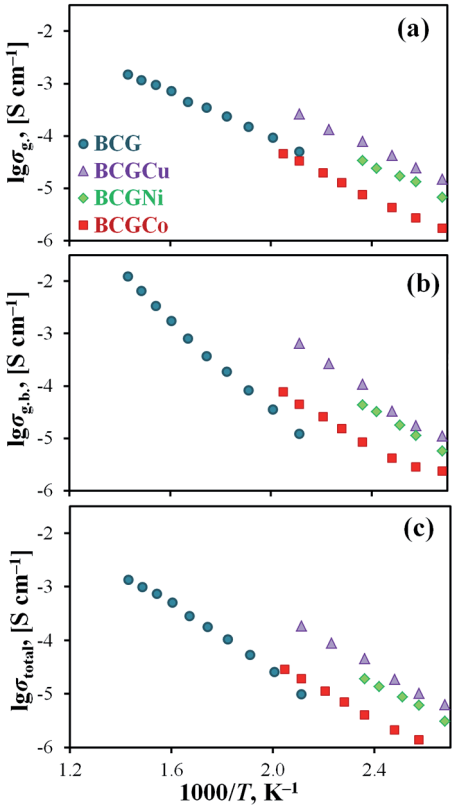

Fig. 4. Grain (a), grain boundary (b) and total (c) conductivities of the BCG and BCGM ceramic materials

As shown in Fig. 5, the apparent activation energies (E_a) of $\sigma_{g.}$ fall in the range of 0.45–0.49 eV, being in close agreement with a characteristic value of 0.5 eV for proton transportation of PCOs [22–24]. According to these data, the M-doping does not affect the grain transport properties of BCG. Another scenario is observed for the grain boundary transport properties, when E_a of $\sigma_{g.b.}$ decreases by 25–40% comparatively 0.92 eV reaching for the basic BCG oxide. It might be also associated with the meaningful decrease of grain boundary density serving as a barrier to ionic charge transfer.

Fig. 6 displays the most interesting result — a ratio between the grain boundary ($R_{g.b.}$) and total (R_{total}) resistances of BCG and BCGM. This ratio decreases significantly for the latter samples as a result of weakening the effect of grain boundaries on the overall transport of BCGM. A vivid example can be seen when $R_{g.b.}/R_{total}$ = = 0.5: for BCG this level is reached at ~250 °C, whereas for BCGM — at 100–125 °C. In terms of real operation of PCOs (400–600 °C), the introduction of 3d-elemetns in small amounts can improve the out-

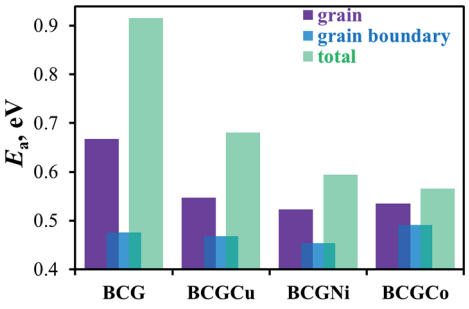

Fig. 5. Apparent activation energy values calculated for different types of conductivities

put properties (power density, current density) of PCO-based electrochemical devices by tens of percent.

Considering transport properties of BCGM and data on low-melting phases in corresponding systems [25–27], it can be concluded that the studied dopants behave differently respectively each other. For example, cobalt is assumed to act as a dopant, fully incorporated in the Ce-site of $BaCeO_3$; nickel is mostly localizes at grain boundary region due to the mentioned low solubility in the Ce-sublattice, although a certain amount can be nonetheless incorporated; finally, copper demonstrates dual nature: it has a high solubility (at least, more than 5 mol.% [21]), but can be also formed as a sediment at grain boundaries because of very low melting temperatures detected for a Ba–Cu–O system [15, 27].

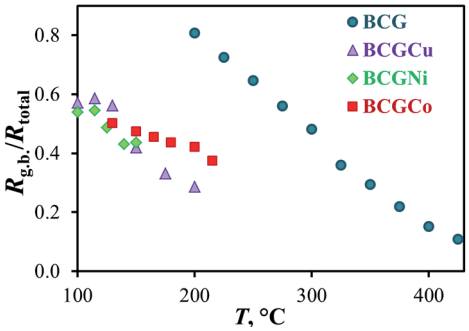

Fig. 6. Temperature dependence of grain boundary resistance contribution of the total resistance of the BCG and BCGM ceramic materials

Conclusions

This work shows that the doping strategy of barium cerate with transition elements is one of the simplest and most effective methods aimed at fabricating the gas-tight ceramic samples at reduced sintering temperatures. This effect is achieved due to the intensification of diffusion processes caused by the appearance of a liquid phase. The latter leads not only to an increase in the relative density of the ceramic materials, but also to grain size growth, which may be favorable for designing new polycrystalline materials and rational engineering their grain boundary parameters.

Acknowledgements

This study was performed within the framework of the Russian Science Foundation [grant no. 18-73-00001].

The characterization of powder and ceramic materials was carried out at the Shared Access Centre “Composition of Compounds” of the Institute of High Temperature Electrochemistry [28].

References

1. Meng Y, Gao J, Zhao Z, Amoroso J, Tong J, Brinkman KS. Review: recent progress in low-temperature proton-conducting ceramics. J Mater Sci. 2019;54(13):9291–312. DOI: 10.1007/s10853-019-03559-9.
2. Kim J, Sengodan S, Kim S, Kwon O, Bu Y, Kim G. Proton conducting oxides: A review of materials and applications for renewable energy conversion and storage. Renew Sustain Energy Rev. 2019;109:606–18 DOI: 10.1016/j.rser.2019.04.042.

3. Mohd Rashid NLR, Samat AA, Jais AA, Somalu MR, Muchtar A, Baharuddin NA, Wan Isahak WNR. Review on zirconate-cerate-based electrolytes for proton-conducting solid oxide fuel cell. Cerm Int. 2019;45(6)6605–15.
DOI: 10.1016/j.ceramint.2019.01.045.
4. Putilov LP, Tsidilkovski VI. Impact of bound ionic defects on the hydration of acceptor-doped proton-conducting perovskites. Phys Chem Chem Phys. 2019;21(12):6391–406.
DOI: 10.1039/C8CP07745B.
5. Wang W, Medvedev D, Shao Z. Gas humidification impact on the properties and performance of perovskite-type functional materials in proton-conducting solid oxide cell. Adv Funct Mater. 2018;28(48):1802592.
DOI: 10.1002/adfm.201802592.
6. Putilov LP, Demin AK, Tsidilkovski VI, Tsiakaras P. Theoretical modeling of the gas humidification effect on the characteristics of proton ceramic fuel cells. Appl Energy. 2019;242:1448–59.
DOI: 10.1016/j.apenergy.2019.03.096.
7. Tarutin A, Lyagaeva J, Farlenkov A, Plaksin S, Vdovin G, Demin A, Medvedev D. A reversible protonic ceramic cell with symmetrically designed $Pr_2NiO_{4+\delta}$-based electrodes: fabrication and electrochemical features. Materials. 2019;12(1):118.
DOI: 10.3390/ma12010118.
8. Danilov N, Lyagaeva J, Vdovin G, Medvedev D. Multifactor performance analysis of reversible solid oxide cells based on proton-conducting electrolytes. Appl Energy. 2019;237:924–34.
DOI: 10.1016/j.apenergy.2019.01.054.
9. Volkov A, Gorbova E, Vylkov A, Medvedev D, Demin A, Tsiakaras P. Design and applications of potentiometric sensors based on proton-conducting ceramic materials. A brief review. Sens Actuators B. 2017;244:1004–15.
DOI: 10.1016/j.snb.2017.01.097.
10. Dai H, Kou H, Wang H, Bi L. Electrochemical performance of protonic ceramic fuel cells with stable $BaZrO_3$-based electrolyte: A mini-review. Electrochem Commun. 2018;96:11–5.
DOI: 10.1016/j.elecom.2018.09.00.
11. Yang L, Wang S, Blinn K, Liu M, Liu Z, Cheng Z, Liu M. Enhanced sulfur and coking tolerance of a mixed ion conductor for SOFCs: $BaZr_{0.1}Ce_{0.7}Y_{0.2-x}Yb_xO_{3-\delta}$. Science. 2009;326(5949):126–9.
DOI: 10.1126/science.1174811.
12. Lee YH, Chang I, Cho GY, Park J, Yu W, Tanveer WH, Cha SW. Thin film solid oxide fuel cells operating below 600°C: a review. Int J Precis Eng Manuf. 2018;5(3):441–53.
DOI: 10.1007/s40684-018-0047-0.
13. Cho GY, Lee YH, Cha SW. Thin film process for thin film solid oxide fuel cells — a review. J Korean Soc Precis Eng. 2018;35(12):1119–29.
DOI: http://dx.doi.org/10.7736/KSPE.2018.35.12.1119.
14. Kjølseth C, Fjeld H, Prytz Ø, Dahl PI, Estournès C, Haugsrud R, Norby T. Space-charge theory applied to the grain boundary impedance of proton conducting $BaZr_{0.9}Y_{0.1}O_{3-\delta}$. Solid State Ionics. 2010;181(5–7):268–75.
DOI: 10.1016/j.ssi.2010.01.014.

15. German RM, Suri P, Park SJ. Review: liquid phase sintering. J Mater Sci. 2009;44(1):1–39. DOI: 10.1007/s10853-008-3008-0.
16. Tong J, Clark D, Bernau L, Subramaniyan A, O'Hayre R. Proton-conducting yttrium-doped barium cerate ceramics synthesized by a cost-effective solid-state reactive sintering method. Solid State Ionics. 2010;181(33–34):1486–98. DOI: 10.1016/j.ssi.2010.08.022.
17. Yun DS, Kim J, Kim S-J, Lee J-H, Kim J-N, Yoon HC, Yu JH, Kwak M, Yoon H, Cho Y, Yoo C-Y. Structural and electrochemical properties of dense yttria-doped barium zirconate prepared by solid-state reactive sintering. Energies. 2018;11(11):3083. DOI: 10.3390/en11113083.
18. Fang S, Wang S, Brinkman KS, Su Q, Wang H, Chen F. Relationship between fabrication method and chemical stability of Ni–$BaZr_{0.8}Y_{0.2}O_{3-\delta}$ membrane. J Power Sources. 2015;278:614–22. DOI: 10.1016/j.jpowsour.2014.12.108.
19. Narendar N, Mather GC, Diasa PAN, Fagg DP. The importance of phase purity in Ni–$BaZr_{0.85}Y_{0.15}O_{3-\delta}$ cermet anodes — novel nitrate-free combustion route and electrochemical study. RSC Adv. 2013;3(3):859–69. DOI: 10.1039/C2RA22301E.
20. Han D, Otani Y, Noda Y, Onishi T, Majima M, Uda T. Strategy to improve phase compatibility between proton conductive $BaZr_{0.8}Y_{0.2}O_{3-\delta}$ and nickel oxide. RSC Adv. 2016;6(23):19288–97. DOI: 10.1039/C5RA26947D.
21. Ananyev M, Medvedev D, Gavrilyuk A, Mitri S, Demin A, Malkov V, Tsiakaras P. Cu and Gd co-doped $BaCeO_3$ proton conductors: experimental vs SEM image algorithmic-segmentation results. Electrochim Acta. 2014;125:371–9. DOI: 10.1016/j.electacta.2013.12.161.
22. Kreuer KD. Proton-conducting oxides. Annu Rev Mater Res. 2003;33:333–59. DOI: 10.1146/annurev.matsci.33.022802.091825.
23. Malavasi L, Fisher CAJ, Islam MS. Oxide-ion and proton conducting electrolyte materials for clean energy applications: structural and mechanistic features. Chem Soc Rev. 2010;39(11):4370–87. DOI: 10.1039/B915141A.
24. Kochetova N, Animitsa I, Medvedev D, Demin A, Tsiakaras P. Recent activity in the development of proton-conducting oxides for high-temperature applications. RSC Adv. 2016;6(77):73222–68. DOI: 10.1039/C6RA13347A.
25. Lander JJ. The phase system BaO–NiO. J Am Chem Soc. 1951;73(6):2450–2. DOI: 10.1021/ja01150a012.
26. Klinkova LA, Nikolaichik VI, Barkovskii NV, Fedotov VK. New phases in the barium-rich region of the BaO–$BaCuO_2$ system. Bull Russ Acad Sci: Phys. 2009;73(8):1104–6. DOI: 10.3103/S1062873809080243.
27. Zhang W, Osamura K, Ochiai S. Phase diagram of the BaO–CuO binary system. J Am Ceram Soc. 1990;73(7):1958–64. DOI: 10.1111/j.1151–2916.1990.tb05252.x
28. http://www.ihte.uran.ru/?page_id=3142.